Flow and penetration behavior of submerged side-blown gas

Shuai Zhu, Qiuyue Zhao, Xiaolong Li, Yan Liu, Tianci Li, and Ting'an Zhang

View the article online at SpringerLink or IJMMM Webpage.

Articles you may be interested in

Min-nan Feng, Yu-cong Wang, Hao Wang, Guo-quan Liu, and Wei-hua Xue, Reconstruction of three-dimensional grain structure in polycrystalline iron via an interactive segmentation method, *Int. J. Miner. Metall. Mater.*, 24(2017), No. 3, pp. 257-263. https://doi.org/10.1007/s12613-017-1403-8

Fei Zhao, Rong Zhu, and Wen-rui Wang, Characteristics of a coherent jet enshrouded in a supersonic fuel gas, *Int. J. Miner. Metall. Mater.*, 27(2020), No. 2, pp. 173-180. https://doi.org/10.1007/s12613-019-1928-0

Gang Niu, Yin-li Chen, Hui-bin Wu, Xuan Wang, and Di Tang, Corrosion behavior of high-strength spring steel for high-speed railway, *Int. J. Miner. Metall. Mater.*, 25(2018), No. 5, pp. 527-535. https://doi.org/10.1007/s12613-018-1599-2

Yong Li, Min-dong Chen, Jian-kuan Li, Long-fei Song, Xin Zhang, and Zhi-yong Liu, Flow-accelerated corrosion behavior of 13Cr stainless steel in a wet gas environment containing CO_2, *Int. J. Miner. Metall. Mater.*, 25(2018), No. 7, pp. 779-787. https://doi.org/10.1007/s12613-018-1626-3

Bao-hua Yang, Ai-xiang Wu, Guillermo A. Narsilio, Xiu-xiu Miao, and Shu-yue Wu, Use of high-resolution X-ray computed tomography and 3D image analysis to quantify mineral dissemination and pore space in oxide copper ore particles, *Int. J. Miner. Metall. Mater.*, 24(2017), No. 9, pp. 965-973. https://doi.org/10.1007/s12613-017-1484-4

Dong-tao Wang, Hai-tao Zhang, Lei Li, Hai-lin Wu, Ke Qin, and Jian-zhong Cui, The evolution of microstructure and mechanical properties during high-speed direct-chill casting in different Al-Mg₂Si *in situ* composites, *Int. J. Miner. Metall. Mater.*, 25(2018), No. 9, pp. 1080-1089. https://doi.org/10.1007/s12613-018-1659-7

IJMMM WeChat   QQ author group

Flow and penetration behavior of submerged side-blown gas

Shuai Zhu[1,2], *Qiuyue Zhao*[1,2], *Xiaolong Li*[1,2], *Yan Liu*[1,2], *Tianci Li*[1,2], *and Ting'an Zhang*[1,2],✉

1) Key Laboratory of Ecological Metallurgy of Multi-metal Intergrown Ores of Ministry of Education, Shenyang 110819, China

2) School of Metallurgy, Northeastern University, Shenyang 110819, China

Abstract: To assess the widely used submerged side-blowing in pyrometallurgy, a high-speed camera–digital image processing–statistical approach was used to systematically investigate the effects of the gas flow rate, nozzle diameter, and inclination angle on the space–time distribution and penetration behavior of submerged side-blown gas in an air–water system. The results show that the gas motion gradually changes from a bubbling regime to a steady jetting regime and the formation of a complete jet structure as the flow rate increases. When the flow rate is low, a bubble area is formed by large bubbles in the area above the nozzle. When the flow rate and the nozzle diameter are significant, a bubble area is formed by tiny bubbles in the area above the nozzle. The increased inclination angle requires a more significant flow rate to form a complete jet structure. In the sampling time, the dimensionless horizontal and vertical penetration depths are Gaussian distributed. Decreasing the nozzle diameter and increasing the flow rate or inclination angle will increase the distribution range and discreteness. New correlations for a penetration depth with an error of ±20% were obtained through dimensional analysis. The dimensionless horizontal penetration depth of an argon-melt system in a 120 t converter calculated by the correlation proposed by the current study is close to the result calculated by a correlation in the literature and a numerical simulation result in the literature.

Keywords: submerged side-blowing; jet; high-speed camera; image processing; dimensional analysis

1. Introduction

Submerged side-blown techniques have been widely used in pyrometallurgy, including the Peirce–Smith converter (PSC) used in copper smelting [1], the side-blown bath smelting process used in lead or zinc smelting [2], and oxygen-rich side-blown bath smelting processes such as the Vanyukov furnace [3–5], argon-oxygen decarburization (AOD) converter [6], and smelting reduction ironmaking processes [7]. The gas blown into the melting bath can react with the melt and provide kinetic energy to stir the melt. The enormous interfacial area between the gas and melt improves the mass and heat transfer and accelerates physical chemistry reactions [8–9]. Thus, the behavior of the gas in the melt significantly impacts metallurgical reactions and bath mixing [10]. Furthermore, the morphology and penetration behavior of submerged side-blown gas significantly affect the gas–liquid interaction and the erosion of the refractory materials [11–12].

Several works have been reported on the submerged side-blown technique. Chibwe *et al.* [13] and Kapusta [14] studied the gas penetration behavior in copper smelting. Their results showed that the gas under the jetting regime could achieve a more extended trajectory and slow refractory erosion. Xiao *et al.* [15] used numerical simulation to study copper smelting. Their results showed that the periodic growth and rise of the bubbles at the nozzle changed the gas

penetration depth. Liu *et al.* [16] used physical and numerical simulations to study lead smelting. Their results showed that the gas penetration depth was not sensitive to the submerged depth of the nozzle. Svantesson *et al.* [17] used numerical simulation to study the gas flow behavior in air–water and IronArc process systems. Their results showed that the incompressible and compressible models overestimated and underestimated the penetration depth by approximately 8.3% and 7.8%, respectively, compared with the results of a correlation proposed by Hoefele and Brimacombe [18]. Significant bubbling and pulsating behavior occurred when the modified Froude number (Fr') was below the transition region. Bölke *et al.* [19–20] studied the gas penetration behavior in the IronArc process. The penetration depth at the centerline of the tuyere oscillated continuously, and the length difference of the oscillation increased with increasing flow rate. The numerical simulation results showed that both the Volume of Fluid and Eulerian–Eulerian models could accurately predict the penetration depth. Wei *et al.* [21] used physical and numerical simulations to study the impact characteristics of submerged gas injection in an electric arc furnace. Their results showed that the inclination angle of the nozzle and the flow rate had a significant effect on the gas behavior. Ma *et al.* [22] experimentally studied the trajectory of side-blown gas. Their results showed that the experimental results agreed with the results of the mathematical model they established. Harby *et al.* [23] found that nozzle diameter

 Springer

and Fr' had a significant effect on both the instability of the jet interface and the penetration behavior. Shi *et al.* [24–25] experimentally studied the flow pattern in the process of jet development. Their results showed that momentum jet, buoyant jet, and plume flow patterns existed along the downstream distance. Li *et al.* [26] experimentally studied the penetration behavior of a steam–air mixture jet in water. Their results showed that increasing the inlet pressure or decreasing the air mass fraction could increase the penetration depth. There have also been some studies on gas motion in AOD converters [27–36]. Wei *et al.* [27–29] used physical simulations to study the flow behaviors within 18 t and 120 t AOD converters. Their results showed that when the flow rate was certain, increasing the number of tuyeres decreased the flow rate and horizontal penetration depth of a single tuyere, which moved the high-temperature zone toward the sidewall around the tuyere. Bjurström *et al.* [32] experimentally found that the penetration depth at the tuyere and liquid surface was strongly affected by the flow rate. The bath depth had little effect on the penetration depth. Odenthal *et al.* [33] found that the penetration depth of the inert gas in the melt could be well approximated by the correlation proposed by Hoefele and Brimacombe [18]. The gas penetration depth obtained by the simulation agreed with the theoretical calculation. Ternstedt *et al.* [35] experimentally found that increasing the flow rate or decreasing the nozzle size resulted in a linear increase in the relative gas penetration depth. Chanouian *et al.* [36] experimentally found that the inclination angle of the converter did not affect the gas penetration depth.

Given the vital role of the submerged side-blown technique in pyrometallurgy, the current work systematically investigated the effects of nozzle diameter (d_n), gas flow rate (Q), and inclination angle of the nozzle (β) on the space–time distribution and penetration behavior of gas in an air–water system. An experimental method of high-speed camera–digital image processing–statistics was used to systematically and quantitatively study the space–time distribution and penetration depth of submerged side-blown gas. In addition, the time-averaged images of the gas–liquid interaction were obtained by the digital image processing method. Compared with the gas–liquid interaction at a certain moment, it is more reasonable to use the time-averaged image to describe the gas–liquid interaction. Moreover, Fr' was studied over a larger range (75–18328), and the time-averaged image clearly showed a significant difference between the bubbling and steady jetting regimes. Finally, the mathematical relationships between dimensionless numbers and the gas penetration depth (L) were established. The obtained new correlation was also compared with the correlation in the literature and the numerical simulation result of the related process. This study has significance for further understanding the mechanism of gas–liquid interactions in pyrometallurgy.

2. Experimental

2.1. Experimental setup

This experiment was carried out in an acrylic tank with dimensions of 0.50 m × 0.30 m × 0.45 m. The experimental system and equipment dimensions are shown in Fig. 1. The installation height and submerged depth of the nozzle were 0.15 m and 0.06 m, respectively. The liquid surface height was 0.25 m, and the liquid depth above the nozzle was 0.10 m. The physical properties of the air–water system used in the experiments and the argon–steel system commonly used in steelmaking are shown in Table 1.
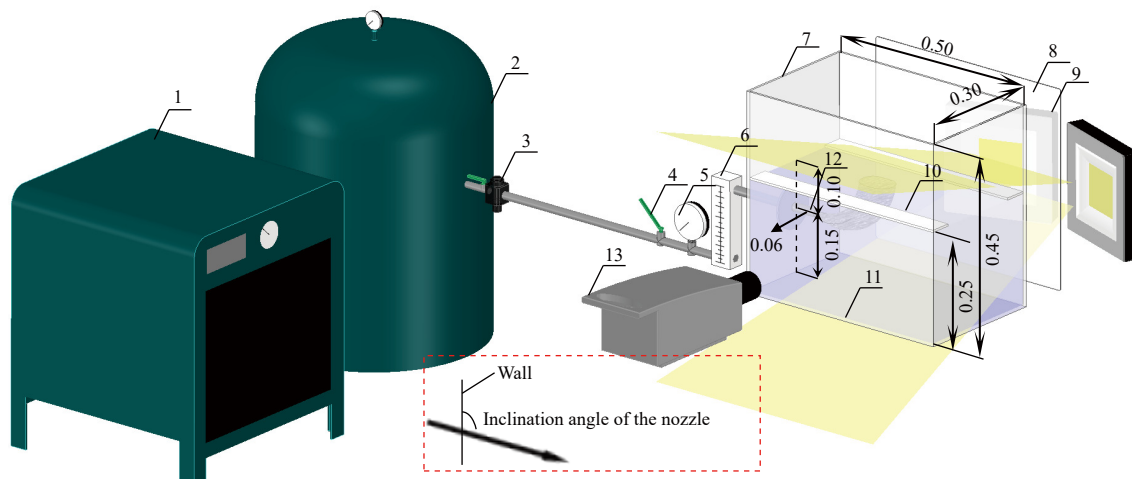

Fig. 1. Experimental system and equipment dimensions (unit: m). 1—Air compressor; 2—Air storage tank; 3—Pressure maintaining valve; 4—Valve; 5—Pressure gauge; 6—Airflow meter; 7—Acrylic tank; 8—Optical diffuser; 9—LEDs; 10—Baffles; 11—Water; 12—Nozzle; 13—High-speed camera.

Table 1. Physical properties of the experimental and high-temperature systems

System	Liquid density, ρ_l / (kg·m^{-3})	Gas density, ρ_g / (kg·m^{-3})	Liquid viscosity, μ_l / (Pa·s)	Surface tension, σ / (N·m^{-1})
Air–water	998	1.205	0.001	0.072
Argon–melt [33,36–37]	7033	1.784	0.0065	1.82

A high-speed camera (Olympus, i-SPEED 3, UK, 1280 pixel × 1024 pixel) was used. Due to the large size of the tank, two LEDs were used to extend the light distribution. A light diffuser was set up between the tank and the LEDs to make the light uniform. Q could be controlled by the valve, pressure gauge, and flow meter, which in turn allowed us to obtain the volumetric flow rate in the normal state. The experiments were performed at approximately 20°C. Under experimental conditions with a high Q, the liquid surface would shake violently. The periodic shaking of the liquid surface caused periodic missing of the gas flow structure, which greatly affected the integrity and continuity of the image recording. Therefore, this problem was solved by installing baffles on both sides above the liquid surface. Since the gas flowed in the middle of the tank and overflowed at the free liquid surface, the presence of the baffles had little effect on the flow state of the gas.

2.2. Experimental parameters

The experimental parameters are summarized in Table 2. The gas flow rates in Table 2 are the values in the normal state. An extensive range of Q was selected to investigate the transition of the gas from the bubbling to the steady jetting regime. A schematic diagram of β is shown in Fig. 1.

Table 2.   Summary of experimental parameters

Parameter	Values
Nozzle diameter, d_n / (10^{-3} m)	3.00, 3.75, 4.50
Volume flow rate of air, Q / (m³·h⁻¹)	3.0, 6.5, 10.0, 13.5, 17.0
Inclination angle of the nozzle, β / (°)	90, 100, 110

2.3. Measurement of gas flow patterns and related parameters

When the experimental system was operating stably, the motion state of the gas was generally stable. However, random motion also occurred continuously, which meant that the gas would move in a specific spatial range as time progressed. Therefore, studying the gas motion state only at a specific moment does not provide accurate information on

the gas–liquid interaction. For the above reasons, the current work combined the methods proposed by Ma *et al.* [22], Harby *et al.* [23], and Dong *et al.* [38] to describe the flow state of the gas using both statistical and summation methods. The images were recorded at a frequency of 500 frame/s for 6 s with a total of 3000 images (the sample size is large enough). Each centimeter corresponds to 23.65 pixels.

Fig. 2 shows the processing of the experimental result. MATLAB was used for programming and image processing. The entire gas information in space was maintained to the maximum extent. The specific process was as follows: (1) read the original image into the program and convert it into a binary image; (2) perform a median filter operation on the binary image to filter out the background noise; (3) save the pixel matrix of the median filter image; (4) process the 3000 original images under this experimental condition in turn and sum the pixel matrix of the 3000 median filter images to obtain a new matrix; (5) transform the pixel matrix obtained in step (4) into a grayscale image, as shown in Fig. 2(d); and (6) transform the grayscale image into a contour image after grayscale normalization, as shown in Fig. 2(e). In Fig. 2(e), x, and y indicate the position coordinates, and the origin is the center point of the nozzle outlet. It should be noted here that in this paper, the grayscale of the white region in Fig. 2(d) was defined as 0, and the grayscale of the black region was 1. The above is the process of the summation method. The final contour image could quickly analyze the gas distribution and flow state. Some essential parameters, such as the horizontal and vertical penetration depths, could also be obtained. The horizontal penetration depth of gas (L_h) is defined as the farthest distance that the gas can reach along the horizontal line of the center of the nozzle outlet. The vertical penetration depth of the gas (L_v) is defined as the distance of the deepest position the gas can reach in the vertical direction from the horizontal line of the center of the nozzle outlet. The above two penetration depths can also be seen in Fig. 2(e).

The parameters of each image, such as L_h and L_v, were extracted as it was processed. The parameters extracted from 3000 images were averaged. The above is the statistical method. It should be noted that the horizontal coordinates of
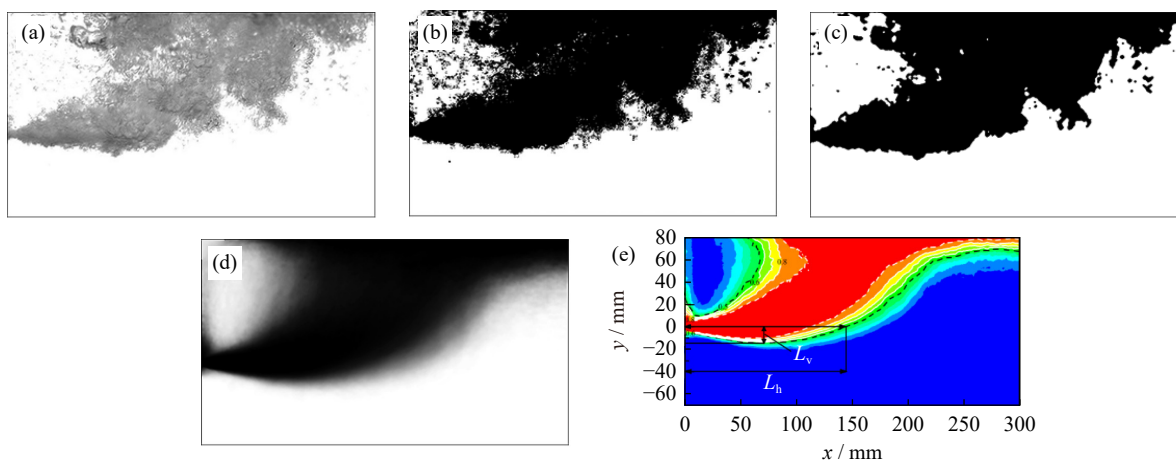

Fig. 2.   Processing of experimental result: (a) original image; (b) binary image; (c) median filter image; (d) sum of 3000 median filter images; (e) contour image.

1070

Int. J. Miner. Metall. Mater., Vol. 30, No. 6, Jun. 2023

the location of L_v in 3000 images are not constant. Therefore, the horizontal coordinate of the location of L_v was first determined in Fig. 2(e). Then, the L_v at that location on each image was extracted using the statistical method.

The numbers in Fig. 2(e) are the values of the grayscale contours. The boundary of L is defined as the location where the contour is 0.5, as shown in Fig. 2(e). The main reason is that the boundary of gas motion is not stable, and the contour of 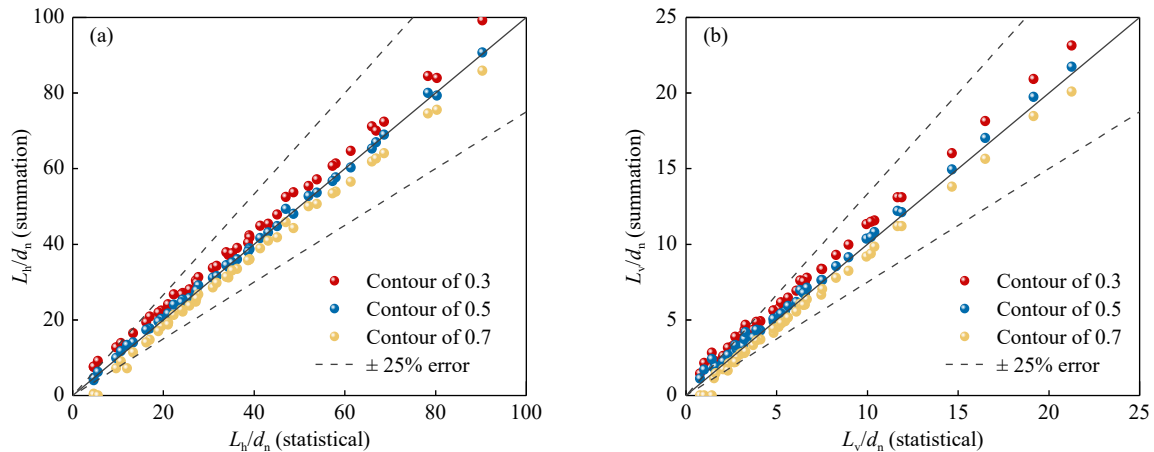0.5 means the "average boundary" of gas motion. After a large number of statistics, the probability that the boundary of gas motion exceeds or does not reach the contour of 0.5 is 0.5, so it is reasonable to use this line as the boundary of L. It can also be seen in Fig. 3 that the error between the summation and the statistical results is very small when the contour of 0.5 is used as the boundary. The error is larger when contours of 0.3 or 0.7 are used as the boundary. The farther the contour is from 0.5, the larger the error between the summation and the statistical results.

Fig. 3. Comparison of the dimensionless penetration depth obtained by the statistical and summation methods, comparing the results of 45 experiments: (a) horizontal direction; (b) vertical direction.

3. Results and discussion

3.1. Space–time distribution state of the gas

Fig. 4 shows the morphology of the gas obtained by the summation method for d_n = 3.00, 3.75, and 4.50 mm at β = 90°. In Fig. 4, Fr' is given for each operating condition. Fr' can be obtained by Eq. (1).

$$Fr' = \rho_g u_g^2 / (\rho_1 - \rho_g) d_n g \tag{1}$$

where u_g is the apparent gas velocity at the nozzle outlet, m·s^{-1}; g is the acceleration of gravity, m·s^{-2}. In general, the colors can be considered as the percentage of time that the gas occupies a specific location during the sampling time, which means that all the regions in the figure, except the blue region, will have gas passing through. The white dashed line is the contour with a grayscale of 0.90, and the black dashed line is the contour with a grayscale of 0.50. First, when d_n is identical, the distribution range of gas increases continuously with increasing Q, and L_h and L_v also increase gradually. Second, when Q is identical, the decreasing d_n will increase the gas distribution range, and L_h and L_v will also gradually increase.

Fig. 4 shows that when $Q \geq 10$ m^3·h^{-1}, the area surrounded by the white dashed line (the red area, i.e., the core region of gas motion) is a complete jet structure. In contrast, when $Q \leq 6.5$ m^3·h^{-1}, especially when $Q = 3.0$ m^3·h^{-1}, the red area is not a complete jet structure. There are two main reasons for producing this incomplete jet structure. First, when $Q \leq 6.5$ m^3·h^{-1}, no matter which d_n is used, the gas velocity is relatively small, resulting in a relatively dispersed distribu-

tion of gas, and only the gas distribution near the nozzle outlet is concentrated. Second, due to the small gas velocity, the gas will quickly change into large bubbles and rise after leaving the nozzle. During image processing, the interior of large bubbles, except for the edges, is often recognized as having the same grayscale as the background liquid, which is one of the reasons for this structure. In general, when $Q \leq 6.5$ m^3·h^{-1}, especially when $Q = 3.0$ m^3·h^{-1}, the motion of the gas is a bubbling or a transition regime, and the steady jetting regime has not yet been reached so that the gas distribution with an incomplete jet structure can occur when $Q \leq 6.5$ m^3·h^{-1}.

It can also be seen in Fig. 4 that under some conditions, the left area of the upper contour with a grayscale of 0.5 (the area above the nozzle) produces the area of a significant bubble. This area decreases as Q increases or d_n decreases. There are two reasons for this phenomenon. First, as shown in Fig. 5(a), the L is small under the bubbling or transition regime when Q is low. The bubble will move upward under the buoyancy quickly after entering the liquid, which causes two results. One is that the upper boundary of the gas movement is not clear. The other is more bubble movement in the area above the nozzle. Thus, the area above the nozzle will produce a significant area of large bubbles at a low Q. Second, as shown in Fig. 5(b), when Q is high, it is in the steady jetting regime. Although there are few large bubbles compared with the lower Q, the gas will expand very quickly after entering the liquid from the nozzle outlet, which causes the generation of many tiny bubbles near the nozzle. During the experiments, it was found that the number of tiny bubbles produced increased with increasing d_n. This resulted in generat-
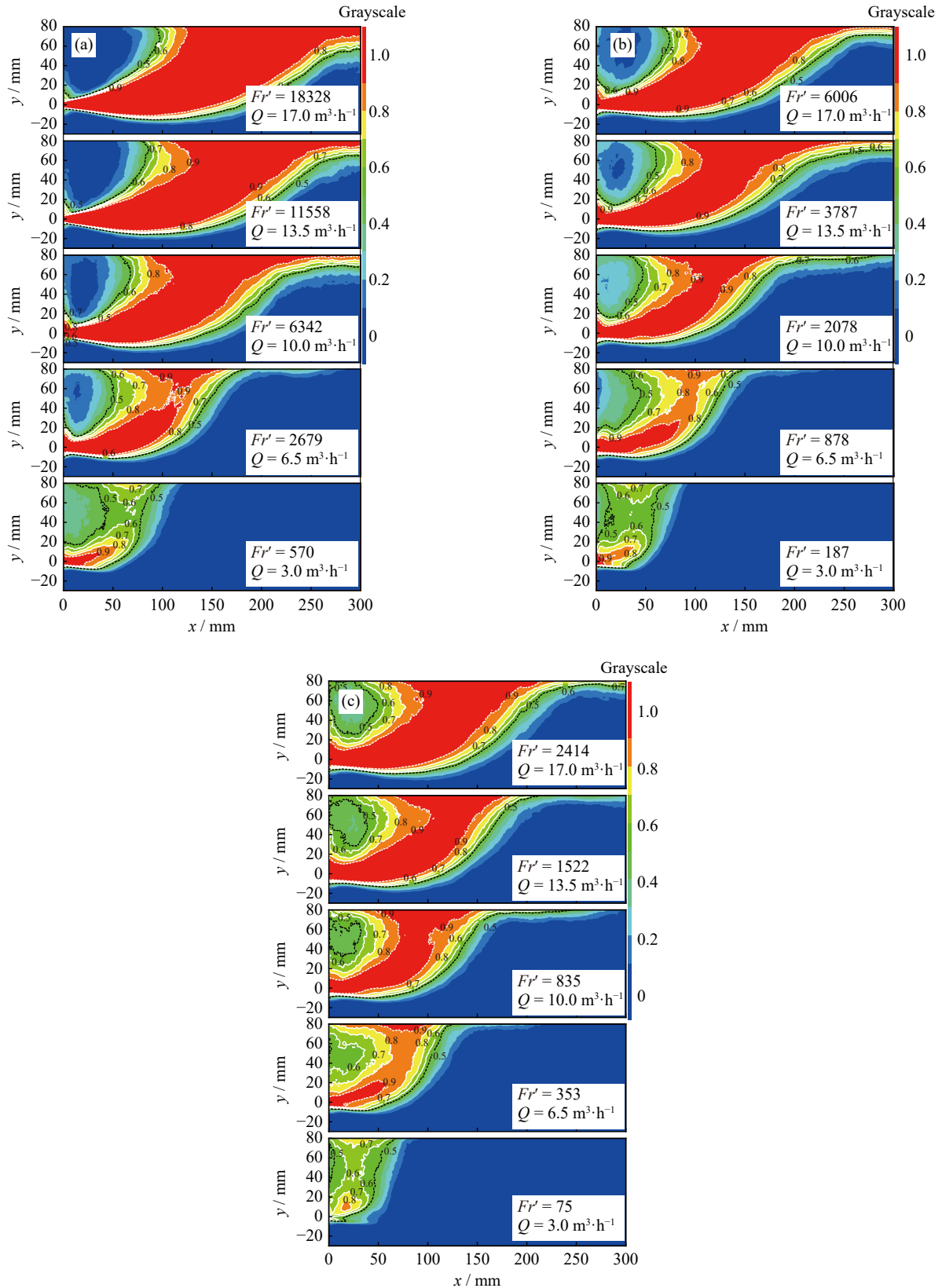
Fig. 4.   Summation results of the morphology of the gas with $\beta = 90°$: (a) $d_n = 3.00$ mm; (b) $d_n = 3.75$ mm; (c) $d_n = 4.50$ mm.

ing a significant area of tiny bubbles above the nozzle at a more significant Q and larger d_n.

Fig. 6 shows the morphology of the gas for $\beta = 100°$ and $110°$ at $d_n = 3.00$ mm. A comparison of Fig. 6 with Fig. 4(a) shows that the gas morphology changes considerably with in-

creasing β. First, when Q is identical, increasing β causes the gas distribution range to be significantly extended. L_h and L_v are also significantly increased, observably extending the trajectory of the gas movement. Second, from the perspective of the core region of gas motion, the cases at $\beta = 90°$ and $100°$

1072

Int. J. Miner. Metall. Mater., Vol. 30, No. 6, Jun. 2023

are relatively similar at identical Q. A relatively complete jet structure is formed when $Q = 10.0$ m³·h⁻¹. When $\beta = 110°$, the gas just began to form a complete jet structure at $Q = 13.5$ m³·h⁻¹. The main reason is that the large β causes the gas to move continuously in the direction of β under the action of kinetic energy. When the kinetic energy is consumed, the bubble on the jet's main body will rise continuously under buoyancy. The bubble relies on buoyancy to rise, and it is challenging to maintain a stable rise path. Furthermore, due to increasing β, the bubble rising distance increases, so it will cause the distribution of bubbles in the rising process to be more dispersed.
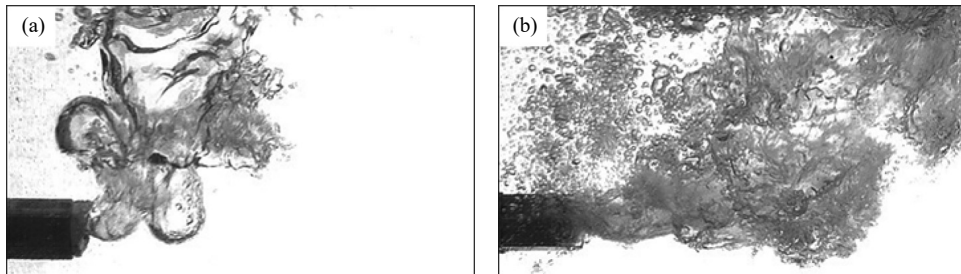

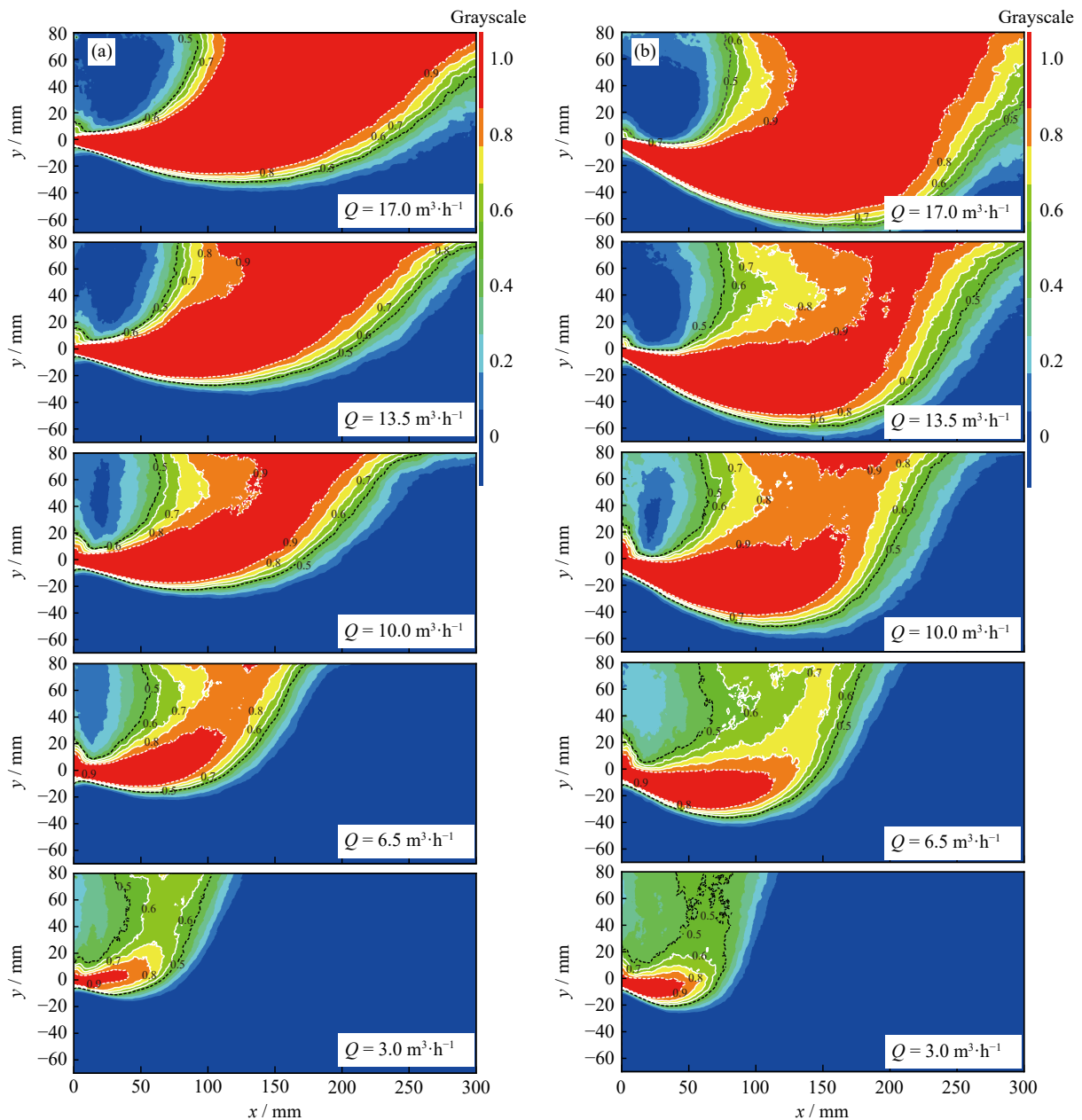Fig. 5.　Gas distribution at different flow rates with $d_n = 3.75$ mm: (a) $Q = 3.0$ m³·h⁻¹; (b) $Q = 10.0$ m³·h⁻¹.

Fig. 6.　Summation results of the morphology of the gas with $d_n = 3.00$ mm: (a) $\beta = 100°$; (b) $\beta = 110°$.

In summary, the effects of d_n, Q, and β on the gas morphology are very significant. With increasing Q, the gas motion state transitions from the bubbling regime to the steady jetting regime. The change in gas morphology is undeniable in this transition process.

3.2. Gas penetration behavior in the horizontal direction

Fig. 7 shows the variation in the dimensionless horizontal penetration depth (L_h/d_n) with Q for $d_n = 3.00$, 3.75, and 4.50 mm at $\beta = 90°$ obtained by the statistical method. First, when d_n is identical, the mean L_h/d_n increases with increasing Q. For example, as Q increases from 3.0 to 17.0 m³·h⁻¹, the mean L_h/d_n increases from 17.0 to 61.3 at $d_n = 3.00$ mm. The distribution range of L_h/d_n during the sampling time increases. The data will become increasingly discrete, which can be seen from the 10%–90% distribution state and the interquartile range (IQR). Second, when Q is identical, the mean L_h/d_n will increase with decreasing d_n. For example, as d_n decreases from 4.50 to 3.00 mm, the mean L_h/d_n increases from 30.9 to 61.3 at $Q = 17.0$ m³·h⁻¹. The distribution range of L_h/d_n increases, and the data become increasingly discrete. Third, it is obvious that the L_h/d_n recorded during the sampling time is Gaussian distributed, and decreasing d_n or increasing Q will expand the distribution range. The variation in the stirring energy (ε) for different conditions can be seen in Fig. 7. ε is important for characterizing the gas–liquid interaction and is given by Eqs. (2)–(4) [39]:

$$\varepsilon = \varepsilon_k + \varepsilon_b = \frac{8\rho_g Q^3}{\pi^2 d_n^4} + NRT_1 \ln \frac{p_1}{p_2} \tag{2}$$

$$\varepsilon_k = \frac{8\rho_g Q^3}{\pi^2 d_n^4} \tag{3}$$

$$\varepsilon_b = NRT_1 \ln \frac{p_1}{p_2} \tag{4}$$

where N is the molar gas flow rate, mol·s⁻¹; R is the gas constant, 8.314 J·mol⁻¹·K⁻¹; T_1 is the temperature of the liquid, K; p_1 is the pressure at the plane where the nozzle is located, Pa; and p_2 is the pressure at the liquid surface, Pa. ε consists mainly of the kinetic energy (ε_k) and the buoyancy energy (ε_b). ε follows the same trend as the L_h, and decreasing d_n or increasing Q will increase ε.
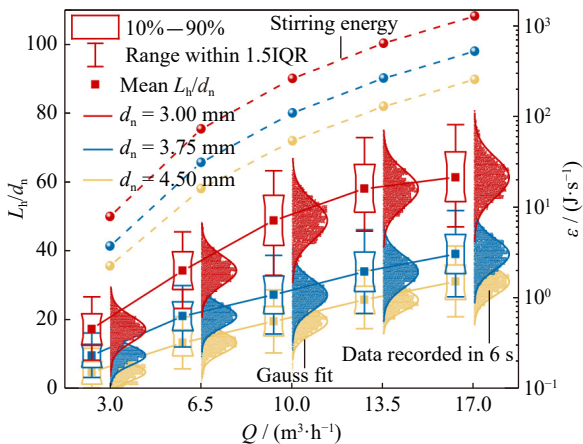
Fig. 8 shows the variation in L_h/d_n with Q for $\beta = 100°$ and 110° at $d_n = 3.00$ mm. Comparing Fig. 8 with the results in Fig. 7 for $d_n = 3.00$ mm and $\beta = 90°$, it is found that the mean L_h/d_n increases with increasing β when Q is identical. For example, as β increases from 90° to 110°, the mean L_h/d_n increases from 61.3 to 90.3 at $Q = 17.0$ m³·h⁻¹. The distribution range of L_h/d_n will increases, and the data become more discrete and Gaussian distributed.

Fig. 8.   Dimensionless horizontal penetration depth vs. gas flow rate with $d_n = 3.00$ mm.

Fig. 9(a) shows the variation in L_h/d_n with the sampling time. It can be found that L_h/d_n oscillates continuously with time, and the results for other conditions are also similar. The time domain signal in Fig. 9(a) is transformed into the frequency domain signal by fast Fourier transform, as shown in Fig. 9(b). To facilitate the analysis, the frequency domain signal in Fig. 9(b) is Gaussian fitted, and the full width at half maximum (FWHM) is obtained, as shown in Fig. 10. First, when d_n is identical, the FWHM shows a general trend of gradually decreasing as Q increases, indicating that the sinusoidal signals constituting the original time domain signal decrease, and the oscillation of L_h/d_n becomes increasingly stable. Second, when Q is identical, the FWHM generally shows a gradually decreasing trend as d_n decreases. Third, when Q is identical, the FWHM generally shows a gradually decreasing trend with increasing β.

3.3. Gas penetration behavior in the vertical direction

This section focuses on the effect of β on the dimensionless vertical penetration depth (L_v/d_n). Fig. 11 shows the variation in L_v/d_n with Q for $\beta = 90°$, 100°, and 110° at $d_n = 3.00$ mm. The results are similar to the situation of L_h/d_n. First, when β is identical, the mean L_v/d_n almost becomes increasingly larger with increasing Q. For example, as Q increases from 3.0 to 17.0 m³·h⁻¹, the mean L_v/d_n increases from 6.3 to 21.3 at $\beta = 110°$. Second, when Q is identical, the mean L_v/d_n increases with increasing β. For example, as β increases from 90° to 110°, the mean L_v/d_n increases from 5.1 to 21.3 at $Q = 17.0$ m³·h⁻¹. Third, it is evident that the L_v/d_n recorded during the sampling time is generally Gaussian distributed. Increas-

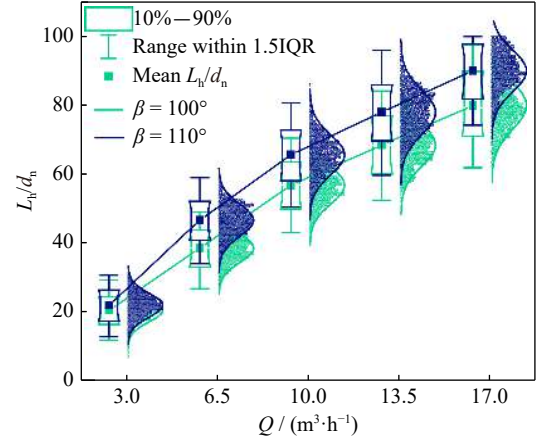**Fig. 7.   Dimensionless horizontal penetration depth and stirring energy vs. gas flow rate with $\beta = 90°$.**

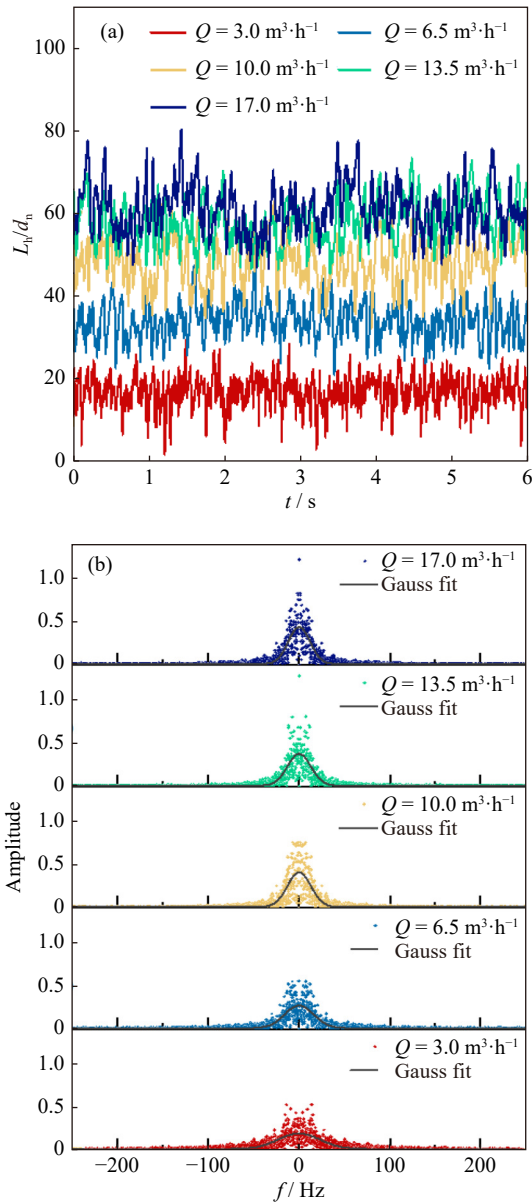**Fig. 9.** (a) Dimensionless horizontal penetration depth vs. time with $d_n = 3.00$ mm and $\beta = 90°$; (b) Frequency domain signal obtained by fast Fourier transform with $d_n = 3.00$ mm and $\beta = 90°$.

ing β or Q will expand the distribution range and increase the discretization degree.

The time domain signal of L_v/d_n is transformed into the frequency domain signal, and then the FWHM is obtained in Fig. 12. First, the FWHM shows a general trend of gradually decreasing as Q increases, indicating that the sinusoidal signals constituting the original time domain signal decrease, and the oscillation process of L_v/d_n becomes increasingly stable. Second, when Q is identical, the FWHM generally shows a gradually decreasing trend with increasing β.

3.4. Empirical correlation of penetration depth

It is important to establish the correlation between L and the relevant parameters. The considered parameters are shown in Table 3 [40]. M, L, and T are the mass, length, and time dimensions, respectively.
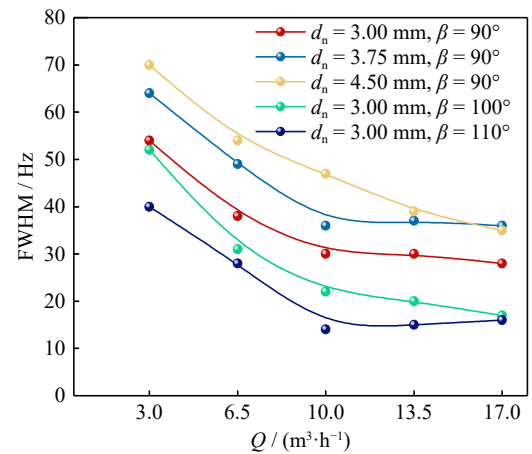

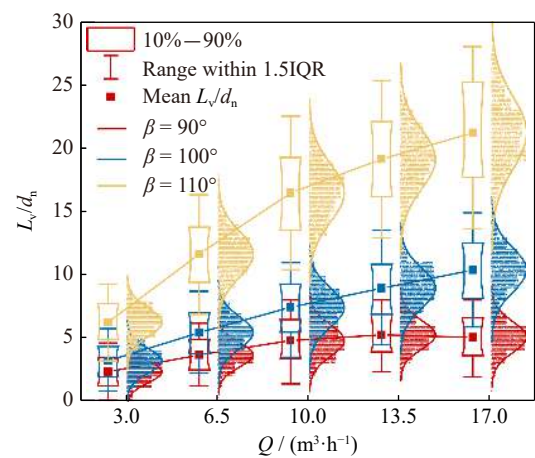**Fig. 10.** Full width at half maximum *vs.* gas flow rate.

Fig. 11. Dimensionless vertical penetration depth vs. gas flow rate with $d_n = 3.00$ mm.
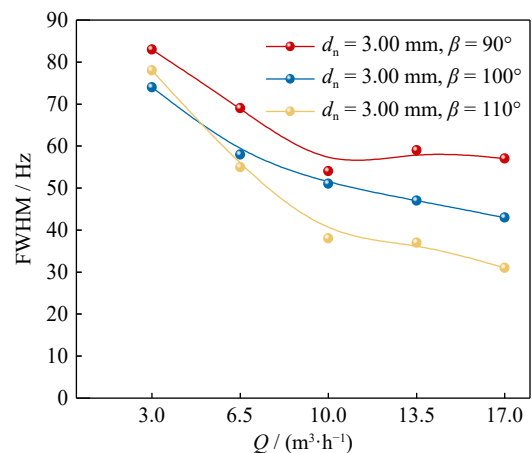

Fig. 12. Full width at half maximum *vs.* gas flow rate.

The apparent gas velocity at the nozzle outlet is

$$u_g = \frac{Q}{\pi(d_n/2)^2} \tag{5}$$

$$f\left(L, \rho_l, \rho_g, g, d_n, u_g, \beta\right) = 0 \tag{6}$$

where ρ_l, u_g, and d_n are selected as independent variables to obtain the expressions for the four dimensionless numbers. The four dimensionless numbers Π_0, Π_1, Π_2, and Π_3 can be

Table 3.   Parameters, symbols, units, and dimensions

Dimension	L / m	ρ_l / (kg·m^{-3})	ρ_g / (kg·m^{-3})	g / (m·s^{-2})	d_n / m	u_g / (m·s^{-1})	β
M	0	1	1	0	0	0	0
L	1	−3	−3	1	1	1	0
T	0	0	0	−2	0	−1	0

obtained by Eqs. (7) to (10), respectively:

$$\Pi_0 = L\rho_1^{a_0}d_n^{b_0}u_g^{c_0} = L/d_n \tag{7}$$

$$\Pi_1 = \rho_g\rho_1^{a_1}d_n^{b_1}u_g^{c_1} = \rho_g/\rho_1 \tag{8}$$

$$\Pi_2 = g\rho_1^{a_2}d_n^{b_2}u_g^{c_2} = gd_n/u_g^2 \tag{9}$$

$$\Pi_3 = \beta\rho_1^{a_3}d_n^{b_3}u_g^{c_3} = \beta \tag{10}$$

$$L/d_n = f_1\left(\rho_g/\rho_1, gd_n/u_g^2, \beta\right) \tag{11}$$

where a_i, b_i, and c_i ($i = 0, 1, 2,$ and 3) are all exponents of independent variables.

Multiple linear regressions were performed on 45 experimental conditions for three d_n (3.00, 3.75, and 4.50 mm), five Q (3.0, 6.5, 10.0, 13.5, and 17.0 m^3·h^{-1}), and three β (90°, 100°, and 110°). The following correlations can be obtained:

$$L_h/d_n = \left(\rho_g/\rho_1\right)^{0.6223}\left(gd_n/u_g^2\right)^{-0.4709}\beta^{1.6534} \tag{12}$$

$$L_v/d_n = \left(\rho_g/\rho_1\right)^{1.0467}\left(gd_n/u_g^2\right)^{-0.3851}\beta^{5.6899} \tag{13}$$

Eq. (12) shows that the effect of β on L_h/d_n is very significant. The appropriate adjustment of β in the smelting process is essential for extending the trajectory of the gas, improving the contact area between the gas and liquid and promoting the reaction. Eq. (13) shows that β has the most significant effect on L_v/d_n.

The relationship between the experimentally obtained results and the calculated results using Eqs. (12) and (13) are plotted in Fig. 13. The errors between the experimental and calculated values are almost all within ±20%, indicating that the accuracy of using Eqs. (12) and (13) to predict L is tolerable. In addition, the current experimental conditions were applied to Eq. (14) proposed by Hoefele and Brimacombe [18]. Fig. 13(a) shows that the majority of the results are within ±20% error. The error between the theoretical values calculated from Eqs. (14) and (12) is small.

$$L_h/d_n = 10.7Fr'^{0.46}\left(\rho_g/\rho_1\right)^{0.35} \tag{14}$$

In addition, the L_h/d_n of gas in a 120 t AOD converter with an operating point of $Fr' = 3268$ was calculated by applying Eq. (12). The physical properties of argon and the melt are shown in Table 1. The calculation was also compared with the results of CFD simulations by Odenthal *et al.* [33] and the calculated results of Eq. (14) [18], as shown in Fig. 14. The result calculated by Eq. (12) is close to the other two results. This study systematically describes the space–time distribution and penetration behavior of submerged side-blown gas, which provides a reference for further understanding the gas–liquid interactions in the AOD converter system as well as in some nonferrous metal smelting reactors.
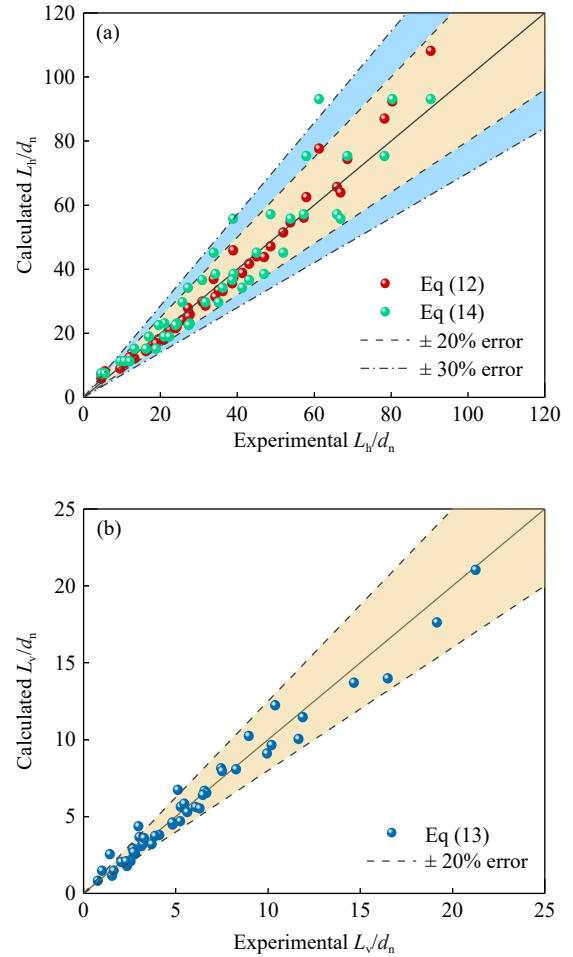

Fig. 13.   Calculated dimensionless penetration depth vs. experimental dimensionless penetration depth: (a) dimensionless horizontal penetration depth; (b) dimensionless vertical penetration depth.
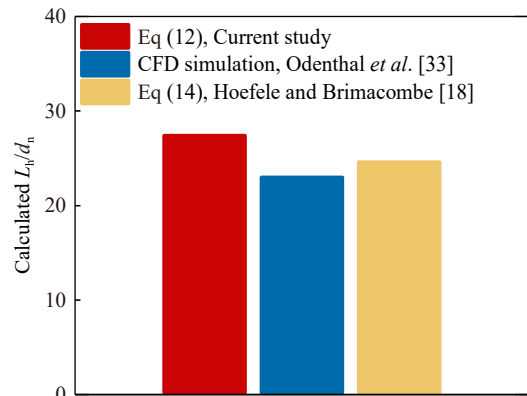

Fig. 14.   Calculated dimensionless horizontal penetration depth of gas in a 120 t AOD converter with d_n = 0.016 m and Fr' = 3268.

1076

Int. J. Miner. Metall. Mater., Vol. 30, No. 6, Jun. 2023

4. Conclusions

The effects of the gas flow rate, nozzle diameter, and inclination angle on the space–time distribution and penetration behavior of submerged side-blown gas were systematically investigated using a high-speed camera–digital image processing–statistics approach in an air–water system. New correlations were established between the relevant dimensionless numbers and gas penetration depth. The main conclusions are as follows.

(1) The results obtained by the summation method indicate that the gas motion gradually changes from a bubbling regime to a steady jetting regime and forms a complete jet structure as the flow rate increases. When the flow rate is low, there is a bubble area formed by large bubbles in the area above the nozzle; when the flow rate and nozzle diameter are more significant, there is a bubble area formed by tiny bubbles in the area above the nozzle. Inclination angle increases will lead to the formation of a complete jet structure requiring a more significant flow rate.

(2) Decreasing the nozzle diameter and increasing the flow rate or inclination angle can increase the mean dimensionless horizontal penetration depth and increase the distribution range and discrete degree of dimensionless horizontal penetration depth in the sampling time. The dimensionless horizontal penetration depth is consistent with the Gaussian distribution.

(3) Increasing the flow rate or inclination angle increases the mean dimensionless vertical penetration depth and increases the distribution range and discrete degree of the dimensionless vertical penetration depth in the sampling time. The dimensionless vertical penetration depth is consistent with Gaussian distribution.

(4) New correlations of the dimensionless horizontal and vertical penetration depths are obtained through dimensional analysis. The error between the calculated and experimental values is within ±20%. The error of the dimensionless horizontal penetration depth calculated from the correlation proposed by the current study and the correlation proposed by Hoefele and Brimacombe is small. The dimensionless horizontal penetration depth in a 120 t converter with an operating point of $Fr' = 3268$ calculated by the correlation proposed by the current study is close to the result calculated by a correlation in the literature and a numerical simulation result in the literature.

Acknowledgements

Conflict of Interest

The authors declare no conflicts of interest.

References

[1] H.L. Zhao, X. Zhao, L.Z. Mu, L.F. Zhang, and L.Q. Yang, Gas-liquid mass transfer and flow phenomena in a Peirce–Smith converter: A numerical model study, *Int. J. Miner. Metall. Mater.*, 26(2019), No. 9, p. 1092.

[2] L. Zhang, L. Zhang, and Y. He, The process and application of oxygen-enriched air side blown smelting of lead–zinc materials, [in] *Proc. 9th International Symposium on Lead and Zinc Processing*, San Diego, 2020, p. 291.

[3] H.L. Zhang, C.Q. Zhou, W. Bing, and Y.M. Chen, Numerical simulation of multiphase flow in a Vanyukov furnace, *J. S. Afr. Inst. Min. Metall.*, 115(2015), No. 5, p. 457.

[4] L. Chen, W.D. Bin, T.Z. Yang, W.F. Liu, and S. Bin, Research and industrial application of oxygen-rich side-blow bath smelting technology, [in] *Proc. 4th International Symposium on High-Temperature Metallurgical Processing*, San Antonio, 2013, p. 49.

[5] L. Chen, W. Chen, H. Xiao, T.Z. Yang, W.F. Liu, and D.C. Zhang, Oxygen-rich side blow bath smelting technology - new developments in China, [in] *Proc. 7th International Symposium on High-Temperature Metallurgical Processing*, Nashville, 2016, p. 123.

[6] J.H. Wei, Y. He, and G.M. Shi, Mathematical modeling of fluid flow in bath during combined side and top blowing AOD refining process of stainless steel: Mathematical model of the fluid flow, *Steel Res. Int.*, 82(2011), No. 6, p. 703.

[7] K.F. Feng, J.Y. Zhang, B. Wang, *et al.*, Numerical simulation study on immersed side-blowing in C–H_2 smelting reduction furnace, [in] *Proc. 5th International Symposium on High-Temperature Metallurgical Processing*, San Diego, 2014, p. 451.

[8] M. Iguchi, S. Kodani, and H. Tokunaga, Bubble and liquid flow characteristics during horizontal cold gas injection into a water bath, *Steel Res. Int.*, 71(2000), No. 11, p. 435.

[9] X.L. Li, Y. Liu, D.X. Wang, and T.A. Zhang, Emulsification and flow characteristics in copper oxygen-rich side-blown bath smelting process, *Metals*, 10(2020), No. 11, art. No. 1520.

[10] R. Cheng, L.J. Zhang, Y.B. Yin, and J.M. Zhang, Effect of side blowing on fluid flow and mixing phenomenon in gas-stirred ladle, *Metals*, 11(2021), No. 2, art. No. 369.

[11] E.P. Heikkinen, T.M.J. Fabritius, T.M.T. Kokkonen, and J.J. Härkki, An experimental and computational study on the melting behaviour of AOD and chromium converter slags, *Steel Res. Int.*, 75(2004), No. 12, p. 800.

[12] K.Z. Song and A. Jokilaakso, Transport phenomena in copper bath smelting and converting processes - A review of experimental and modeling studies, *Miner. Process. Extr. Metall. Rev.*, 43(2022), No. 1, p. 107.

[13] D.K. Chibwe, G. Akdogan, G.A. Bezuidenhout, J. Kapusta, S. Bradshaw, and J.J. Eksteen, Sonic injection into a PGM Peirce-Smith converter: CFD modelling and industrial trials, *J. S. Afr. Inst. Min. Metall.*, 115(2015), No. 5, p. 349.

[14] J.P.T. Kapusta, Submerged gas jet penetration: A study of bubbling versus jetting and side versus bottom blowing in copper bath smelting, *JOM*, 69(2017), No. 6, p. 970.

[15] Y.D. Xiao, T.T. Lu, Y.G. Zhou, Q.Q. Su, L.Z. Mu, T. Wei, H.L. Zhao, and F.Q. Liu, Computational fluid dynamics study on enhanced circulation flow in a side-blown copper smelting furnace, *JOM*, 73(2021), No. 9, p. 2724.

[16] Y.T. Liu, T.Z. Yang, Z. Chen, Z.Y. Zhu, L. Zhang, and Q. Huang, Experiment and numerical simulation of two-phase flow in oxygen enriched side-blown furnace, *Trans. Nonferrous Met. Soc. China*, 30(2020), No. 1, p. 249.

[17] J.L. Svantesson, M. Ersson, and P.G. Jönsson, Effect of Froude number on submerged gas blowing characteristics, *Materials* (*Basel*), 14(2021), No. 3, art. No. 627.

[18] E.O. Hoefele and J.K. Brimacombe, Flow regimes in submerged gas injection, *Metall. Mater. Trans. B*, 10(1979), No. 4, p. 631.

[19] K. Bölke, M. Ersson, P.Y. Ni, M. Swartling, and P.G. Jönsson, Physical modeling study on the mixing in the new IronArc process, *Steel Res. Int.*, 89(2018), No. 7, art. No. 1700555.

[20] K. Bölke, M. Ersson, M. Imris, and P.G. Jönsson, Importance of the penetration depth and mixing in the IRONARC process, *ISIJ Int.*, 58(2018), No. 7, p. 1210.

[21] G.S. Wei, R. Zhu, T.P. Tang, K. Dong, and X.T. Wu, Study on the impact characteristics of submerged CO_2 and O_2 mixed injection (S-COMI) in EAF steelmaking, *Metall. Mater. Trans. B*, 50(2019), No. 2, p. 1077.

[22] J. Ma, Y.P. Song, P. Zhou, W. Cheng, and S.G. Chu, A mathematical approach to submerged horizontal buoyant jet trajectory and a criterion for jet flow patterns, *Exp. Therm. Fluid Sci.*, 92(2018), p. 409.

[23] K. Harby, S. Chiva, and J.L. Muñoz-Cobo, An experimental investigation on the characteristics of submerged horizontal gas jets in liquid ambient, *Exp. Therm. Fluid Sci.*, 53(2014), p. 26.

[24] H.H. Shi, Q. Guo, C. Wang, *et al*., Oscillation flow induced by underwater supersonic gas jets, *Shock Waves*, 20(2010), No. 4, p. 347.

[25] H.H. Shi, B.Y. Wang, and Z.Q. Dai, Research on the mechanics of underwater supersonic gas jets, *Sci. China Phys. Mech. Astron.*, 53(2010), No. 3, p. 527.

[26] W.C. Li, Z.M. Meng, Z.N. Sun, L. Sun, and C. Wang, Investigations on the penetration length of steam–air mixture jets injected horizontally and vertically in quiescent water, *Int. J. Heat Mass Transf.*, 122(2018), p. 89.

[27] J.H. Wei, J.C. Ma, Y.Y. Fan, N.W. Yu, S.L. Yang, S.H. Xiang, and D.P. Zhu, Water modelling study of fluid flow and mixing characteristics in bath during AOD process, *Ironmaking Steelmaking*, 26(1999), No. 5, p. 363.

[28] J.H. Wei, H.L. Zhu, H.B. Chi, and H.J. Wang, Physical modeling study on combined side and top blowing AOD refining process of stainless steel: Fluid mixing characteristics in bath, *ISIJ Int.*, 50(2010), No. 1, p. 26.

[29] J.H. Wei, H.L. Zhu, H.B. Chi, and H.J. Wang, Physical modeling study on combined side and top blowing AOD refining process of stainless steel: Gas stirring and fluid flow characteristics in bath, *ISIJ Int.*, 50(2010), No. 1, p. 17.

[30] T. Fabritius, P. Kupari, and J. Härkki, Physical modelling of a sidewall-blowing converter, *Scand. J. Metall.*, 30(2001), No. 2, p. 57.

[31] T.M.J. Fabritius, P.T. Mure, and J.J. Härkki, The determination of the minimum and operational gas flow rates for sidewall blowing in the AOD-converter, *ISIJ Int.*, 43(2003), No. 8, p. 1177.

[32] M. Bjurström, A. Tilliander, M. Iguchi, and P. Jönsson, Physical-modeling study of fluid flow and gas penetration in a side-blown AOD converter, *ISIJ Int.*, 46(2006), No. 4, p. 523.

[33] H.J. Odenthal, U. Thiedemann, U. Falkenreck, and J. Schlueter, Simulation of fluid flow and oscillation of the argon oxygen decarburization (AOD) process, *Metall. Mater. Trans. B*, 41(2010), No. 2, p. 396.

[34] T. Hass, V.V. Visuri, A. Kärnä, E. Isohookana, P. Sulasalmi, R.H. Eriç, H. Pfeifer, and T. Fabritius, Physical modelling of the effect of slag and top-blowing on mixing in the AOD process, [in] *Proc. 10th International Conference on Molten Slags, Fluxes and Salts*, Seattle, 2016, p. 999.

[35] P. Ternstedt, P.Y. Ni, N. Lundqvist, A. Tilliander, and P.G. Jönsson, A physical modelling study to determine the influence of slag on the fluid flow in the AOD converter process, *Ironmaking Steelmaking*, 45(2018), No. 10, p. 944.

[36] S. Chanouian, B. Ahlin, A. Tilliander, and M. Ersson, Inclination effect on mixing time in a gas–stirred side–blown converter, *Steel Res. Int.*, 92(2021), No. 10, art. No. 2100044.

[37] Y.G. Xu, M. Ersson, and P.G. Jönsson, Numerical investigations on bubble behavior at a steel–slag interface, *Steel Res. Int.*, 91(2020), No. 6, art. No. 1900611.

[38] P. Dong, B.J. Lu, S.F. Gong, and D. Cheng, Experimental study of submerged gas jets in liquid cross flow, *Exp. Therm. Fluid Sci.*, 112(2020), art. No. 109998.

[39] C.J. Su, J.M. Chou, and S.H. Liu, Effect of gas bottom blowing conditions on fluid flow phenomena and mixing time of molten iron inside an ironmaking smelter, *Mater. Trans.*, 51(2010), No. 9, p. 1602.

[40] A.N. Conejo, *Fundamentals of Dimensional Analysis: Theory and Applications in Metallurgy*, Springer Singapore, Singapore, 2021, p. 305.